Influence of Mach number and static pressure on plasma flow control of supersonic and rarefied flows around a sharp flat plate

Sandra Coumar · Viviana Lago

Abstract This paper presents an experimental investigation, carried out at the Icare Laboratory by the FAST team, focusing on plasma flow control in supersonic and rarefied regime. The study analyzes how the Mach number as well as the ambient pressure modify the repercussions of the plasma actuator on the shock wave. It follows previous experiments performed in the MARHy (ex–SR3) wind tunnel with a Mach 2 flow interacting with a sharp flat plate where modifications induced by a plasma actuator were observed. The flat plate was equipped with a plasma actuator composed of two aluminum electrodes. The upstream one was biased with a negative DC potential and thus created a glow discharge type plasma. Experimental measurements showed that the boundary layer thickness and the shock wave angle increased when the discharge was ignited. The current work was performed with two nozzles generating Mach 4 flows but at two different static pressures: 8 Pa and 71 Pa. These nozzles were chosen to study independently the impact of the Mach number and the impact of the pressure on the flow behavior. In the range of the discharge current considered in this experimental work it was observed that the shock wave angle increased with the discharge current $+15\%$ for the Mach 2 flow but the increase rate doubled to $+28\%$ for the Mach 4 flow at the same static pressure showing that the discharge effect is even more significant when boosting the flow speed. When studying the effect of the discharge on the Mach 4 flow at higher static pressure, it was observed that the topology of the plasma changed drastically and the increase in the shock wave angle with the discharge current was $+21\%$.

S. Coumar · V. Lago
ICARE, CNRS, UPR 3021
1C Avenue de la Recherche Scientifique, 45071, Orléans Cedex 2, France
E-mail: sandra.coumar@cnrs-orleans.fr
E-mail: viviana.lago@cnrs-orleans.fr

1 Introduction

During the reentry phase into a dense gas atmosphere, spacecraft flying at hypersonic velocities are exposed to severe conditions and the mission planning must delicately balance three requirements: deceleration, heating management and accuracy of the localization and velocity when landing.

One idea could be to reduce the spacecraft velocity at very high altitudes, and hence decrease the heat load encountered over the trajectory thus leading to the reduction of the thermal protection system and vehicle payload. The requirements of reentry missions strongly depend on the drag force which is the dominant force over all others including gravity and lift. The increase in the wall drag force reduces the velocity of the spacecraft, thereby having a directly beneficial effect on heat loads, vehicle design and re-entry trajectory. At high altitudes, corresponding to rarefied regimes, aerodynamic control is usually fulfilled by thrusters. The implementation of other ways of aerodynamic control could be advantageous because it reduces the amount of fuel to be loaded on board. In this respect, one of the most promising technologies consists in using active flow control methods with plasma-based devices.

It has been demonstrated that plasma actuators offer the possibility to modify the shock wave shape around the vehicle and thus the drag coefficient. Moreover, plasma actuators could help to avoid black-out transmission by using MHD to optimize communication links.

Other ways have been explored such as those proposed by (Zuppardi (2015)). Using a Monte Carlo code, Zuppardi studied the efficiency of a wing-flap in hypersonic and rarefied flow simulating altitudes of 65 and 85 km. The study quantified the effects of the use of wing-flaps and concluded that aerodynamic control seems to be feasible and could also reduce fuel consumption. Nevertheless calculations predict a consistent increment of pressure and heat flux on the lower

surface of the flap, where a thermal protection system is required, meaning an increase in the total aircraft weight.

Compared to traditional flow control methods, plasma actuators present several advantages such as their fast response time, low weight and size and relatively low energy consumption, offering promising applications for flight control systems at high velocities.

A large number of studies have been carried out, evidencing the interest in plasma control research applied to supersonic flow conditions such as Kimmel et al (2004); Kuo and Bivolaru (2007); Kuo (2007); Leonov et al (2005); Leonov and Yarantsev (2008); Leonov (2011) and Starikovskiy and Aleksandrov (2011).

Although many investigations deal with plasma control applied to supersonic flow, only few concern rarefied flows applied to atmospheric re-entries. Shin et al (2007) investigated this kind of flow but without clear evidence of plasma actuation even if they observed two distinct discharge modes. Surzhikov and Shang (2004) conducted very interesting work on the discharge modeling in rarefied regime with external magnetic field conditions but their study focused only on the discharge modeling without analyzing the interaction with a flow. Menart et al (2006) studied the change in lift of a flat plate subjected to a surface discharge in a flow at Mach 5. The pressure in the measuring chamber was 80 Pa and the temperature 42 K. The model was a flat plate with an edge. The upper part was equipped with 2 copper electrodes. The power supply delivered a square-shaped current shape which can be ranged between 8 and 24 mA, the electric powers involved were about $30W$. A change in the lift of the model was measured and was found to be greater as the cathode has a high surface area and even more so when the cathode is situated close to the leading edge. Palm et al (2003) clearly demonstrated some plasma actuation in a rarefied supersonic flow with a model configuration similar to the cylinder model studied by the FAST team in Lago et al (2014). The use of plasma control in atmospheric entries was numerically studied by Poggie et al. Poggie (2005) showed that a DC glow discharge applied over a flat plate at Mach 5 and 650 Pa modified the flow field and increase the pressure forces over the flat plate surface. In a more recent paper, Poggie and Atkinson (Atkinson et al (2013)) explored numerically the efficiency of coupling magnetic forces with plasma actuators acting over a blunt-nose cone at Mach 14 with a view to controlling the stability of the model during atmospheric reentry at high attack angle.

However, hypersonic vehicles are submitted to great variations of the atmosphere and changes in pressure, gas density and sound speed depending on the atmospheric altitude. Each re-entry phase induces various flow conditions around the vehicle which may lead to completely different phenomena when using plasma actuators. Therefore, even if the use of plasma actuators could be in the future an alternative to

complex geometry design for hypersonic vehicles and atmospheric entry probes, recent experiences have demonstrated that there are still improvements to be made and that the underlying physics remains to be elucidated. The specificity of our team is to experimentally simulate supersonic and hypersonic flows at very low pressure which corresponds to the high altitude phase of re-entry trajectories, and hence to provide complementary databases and knowledge with respect to other authors working at higher pressures and thus, higher Reynolds numbers. Whereas other studies aim to decrease drag, and control the boundary layer separation because such studies concern flight conditions at high Reynolds number, our team focuses on spacecraft flying at supersonic and hypersonic velocities at high altitudes where the modification of shock waves aims to increase drag and to improve the control and stability of the vehicle.

This paper follows a study carried out in the MARHy wind-tunnel of ICARE in which a sharp flat plate equipped with a plasma actuator interacts with a Mach 2 flow at a static pressure of 8 Pa. Experimental studies reported in Menier et al (2007), Lago et al (2008) conducted at supersonic and rarefied regime showed that the plasma actuator increases the shock angle. Investigation carried out with the Monte Carlo method showed that this effect is due in part to the surface heating of the flat plate but is not due to ionic wind or volume heating. In Joussot et al (2015) and Joussot and Lago (2016), experiments were carried out with a heater instead of the plasma actuator, in order to quantify the role of the surface heating showing that it accounts for 50% at most. The other 50% is due to the ionization produced by the plasma discharge created by the plasma actuator which modifies the flow properties and the flow interaction with the flat plate. In Coumar et al (2015) and Coumar et al (2016), numerical simulations were carried out with a Navier Stokes code adapted with slip conditions to rarefied regime, to evaluate the drag and lift force. Results showed that a 13% increase in the drag coefficient could be achieved with the plasma actuator in our experimental conditions.

The purpose of the present investigation is to go further and observe how this type of plasma actuator reacts in different flow conditions because during atmospheric re-entry the vehicle will pass through different atmospheric layers with different pressures and Mach numbers. Indeed, the topology of a given discharge strongly depends on the ambient pressure, and its interaction with the flow depends on pressure. To provide some answers, we propose in this paper a comparative study based on the same model and discharge configuration placed in different flow conditions : Mach 2/8 Pa, Mach 4/8 Pa and Mach 4/71 Pa.
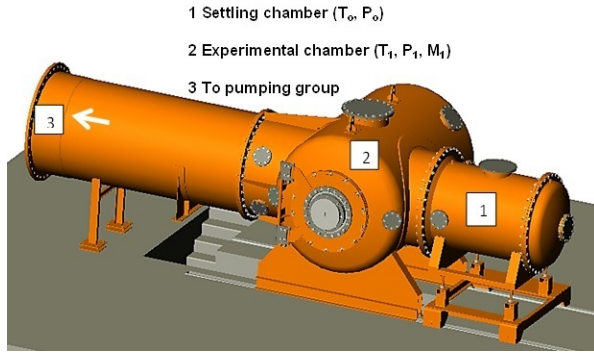
Fig. 1 The Marhy wind tunnel lay-out

2 Experimental setup

2.1 The MARHy wind tunnel

The MARHy low density facility of the ICARE laboratory (CNRS, France) is used for both academic and industrial research. The wind tunnel was built in 1963 at the 'Laboratoire d'Aérothermique' and was known as the 'SR3' wind tunnel (Allègre (1992)) until its relocation in 2006 at the CNRS-Orléans. A schematic view of the facility is presented in Fig. 1. It consists of three main parts: the settling chamber with a diameter of 1.3 m and a length of 2.0 m, the test chamber with a diameter of 2.3 m and a length of 5.0 m, and a third chamber in which a diffuser is installed. The diffuser is connected to the pumping group by a vacuum gate. A powerful pumping group with 2 primary pumps, 2 intermediary Roots blowers and 12 Roots blowers ensures the low density flow conditions in continuous operating mode. Depending on the desired rarefaction level, the number of pumps used can be varied. When supplied with different nozzles, the wind tunnel generates subsonic, supersonic and hypersonic flows from Mach 0.8 to Mach 21, and covers a large range of Reynolds numbers from 10^2 up to 10^5 for a reference length of 100 mm (corresponding to the length of the flat plate used as model).

The present study was carried out with three contoured nozzles, the first one (called N1) gives an air flow at Mach 2 and a static pressure of 8 Pa, the second one (called N2), an air flow at Mach 4 and a static pressure of 8 Pa and third (called N3), an air flow at Mach 4 and a static pressure of 71 Pa. In order to facilitate the understanding of the study, the nozzles will be referred to as N1 (M2 - 8 Pa), N2 (M4 - 8 Pa) and N3 (M4 - 71 Pa) Tables 1-3 compile the overall operating conditions for each nozzle, where p represents the pressure, T the temperature, ρ the volumetric mass density, U the flow velocity, M the Mach number, λ the mean free path and R_{eL} the Reynolds number based on the flat plate length $L = 100$ mm and calculated with the relation $R_e = U_1 L / \mu_1$, where μ_1 is the kinematic viscosity. These three nozzles were chosen to study how the

Table 1 N1 (M2 - 8 Pa) Operating conditions

Stagnation conditions	Free stream conditions
$p_0 = 63\,\text{Pa}$	$p_1 = 8\,\text{Pa}$
$T_0 = 293\,\text{K}$	$T_1 = 163\,\text{K}$
$\rho_0 = 7.44 \times 10^{-4}\,\text{kg·m}^{-3}$	$\rho_1 = 1.71 \times 10^{-4}\,\text{kg·m}^{-3}$
	$\mu_1 = 1.10 \times 10^{-5}\,\text{Pa·s}$
	$U_1 = 511\,\text{m·s}^{-1}$
	$M_1 = 2$
	$\lambda_1 = 0.260\,\text{mm}$
	$R_{eL} = 801\,, L = 100\text{mm}$

Table 2 N2 (M4 - 8 Pa) Operating conditions

Stagnation conditions	Free stream conditions
$p_0 = 1214\,\text{Pa}$	$p_1 = 8\,\text{Pa}$
$T_0 = 293\,\text{K}$	$T_1 = 70\,\text{K}$
$\rho_0 = 1.44 \times 10^{-2}\,\text{kg·m}^{-3}$	$\rho_1 = 3.99 \times 10^{-4}\,\text{kg·m}^{-3}$
	$\mu_1 = 1.10 \times 10^{-5}\,\text{Pa·s}$
	$U_1 = 670\,\text{m·s}^{-1}$
	$M_1 = 4$
	$\lambda_1 = 0.067\,\text{mm}$
	$R_{eL} = 5603\,, L = 100\text{mm}$

Table 3 N3 (M4 - 71 Pa) Operating conditions

Stagnation conditions	Free stream conditions
$p_0 = 10797\,\text{Pa}$	$p_1 = 71\,\text{Pa}$
$T_0 = 293\,\text{K}$	$T_1 = 70\,\text{K}$
$\rho_0 = 0.128 \times 10^{-2}\,\text{kg·m}^{-3}$	$\rho_1 = 3.55 \times 10^{-3}\,\text{kg·m}^{-3}$
	$\mu_1 = 1.10 \times 10^{-5}\,\text{Pa·s}$
	$U_1 = 670\,\text{m·s}^{-1}$
	$M_1 = 4$
	$\lambda_1 = 0.008\,\text{mm}$
	$R_{eL} = 49818\,, L = 100\text{mm}$

plasma discharge modifies the flowfield around the flat plate and thus, the shock wave when the Mach number changes whereas the static pressure remains the same (nozzles N1 (M2 - 8 Pa) and N2 (M4 - 8 Pa)) and then when the static pressure is changed but for the same Mach number (nozzles N2 (M4 - 8 Pa) and N3 (M4 - 71 Pa)). The air flow distributions are uniform through the test sections with a core diameter of 15 cm and a core length of 30 cm for N1 (M2 - 8 Pa), a core diameter of 8 cm and a core length of 20 cm for N2 (M4 - 8 Pa) and a core diameter of 10 cm and a core length of 20 cm for N3 (M4 - 71 Pa). Based on the free-stream conditions, the corresponding geometric altitudes were calculated, giving 67 km for N1 (M2 - 8 Pa), 71.5 km for nozzle N2 (M4 - 8 Pa) and 50 km for nozzle N3 (M4 - 71 Pa).

2.2 Models and plasma actuator

The model under investigation when using N1 (M2 - 8 Pa) is a flat plate (100 mm-long, 80 mm-wide and 4 mm-thick) with a sharp leading edge (15°), as shown on Fig. 2. For nozzles
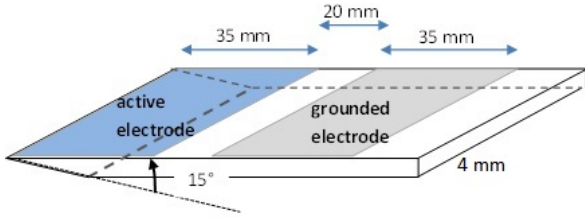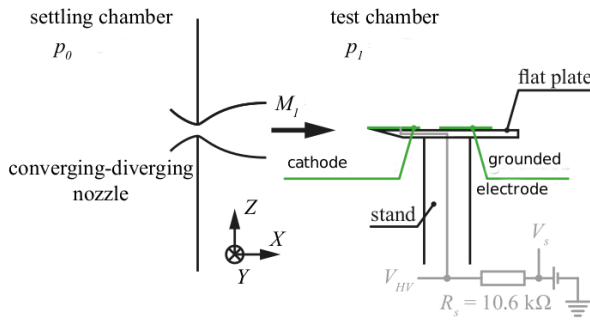
Fig. 2 Scheme of the flat plate/actuator

Fig. 3 Experimental set-up

N2 (M4 - 8 Pa) and N3 (M4 - 71 Pa), the width of the flat plate is reduced to $50\,mm$ because of the smaller core diameters of the flows generated by these nozzles. The models are made of quartz in order to withstand the high surface temperatures reached when using the plasma actuator. The flat plates are placed on a profile stand in the test section, downstream the nozzle exit as sketched on Fig. 3. The plasma actuator is composed of two aluminum electrodes, $80\,mm$ or $50\,mm$-wide depending on the model and $35\,mm$-long, $80\,\mu m$-thick. These electrodes are flush mounted on the upper surface of the flat plate (see Fig. 2). The electrodes size is calculated in order to keep the ratio of the active electrode surface on the model surface constant at 35%. The first electrode, called the active electrode or the cathode, is set at the leading edge of the plate, and is connected to a high voltage DC power supply (Spellman, SR15PN6) through a current limiting resistor ($R_s = 10.6\,k\Omega$), while the second electrode is grounded. The high voltage V_s is fixed with the power supply, which delivers the discharge current I_{HV}. The voltage applied to the active electrode, V_{HV}, is then calculated with the following relation: $V_{HV} = V_s - R_s I_{HV}$. V_s and I_{HV} are read directly on the power supply. This procedure ensures the stability of the discharge conditions. With respect to the size of the models and the nozzle free stream conditions, the Knudsen numbers ($Kn = \lambda_1/L$) are $Kn = 0.003$ for nozzle N1 (M2 - 8 Pa), corresponding to the slip-flow regime or slightly rarefied regime, Kn=7×10^{-4} for nozzle N2 (M4 - 8 Pa) and Kn=8×10^{-5} for nozzle N3 (M4 - 71 Pa) giving a flow close to the continuum regime.

Table 4 Range of pressure sensors for each operating nozzle condition

Pressure measured	N_1	N_2	N_3
p_0	$1\,Torr$	$10\,Torr$	$1000\,Torr$
p_1	$0.1\,Torr$	$0.1\,Torr$	$1\,Torr$
p_{Pitot}	$1\,Torr$	$10\,Torr$	$100\,Torr$

2.3 Diagnostics

2.3.1 Probe pressure measurements

The good operation of the supersonic MARHy wind tunnel is based on accurate measurements of the stagnation and test section pressures. For this purpose these pressures are measured with absolute capacitive sensors (MKS, 600 series Baratron) whose scales are adapted to the range of the measurement values. Table 4 summarizes the scale values of the pressure manometers used for each nozzle condition. The manometers are connected to a MKS control unit (PR 4000B) with a 12-bit resolution. The pressure in the flow above the plate is measured with a Pitot probe connected to a MKS Baratron capacitance manometer (see Table 4) connected to a MKS control unit (PDR-C-2C). A 3-axis traversing system, controlled by a computer, ensures the displacement of the Pitot probe with a step resolution on each axis of $0.1\,mm \pm 0.02\,mm$ on each position. The Pitot probe is made of glass in order to avoid electrical interactions with the discharge. The Pitot tube consists of a flat-ended cylinder with an external diameter of $D = 6\,mm$ and an internal diameter of $d = 4\,mm$. Given this to these dimensions and the free-stream flow conditions (see Tables 1-3), it is not necessary to apply viscous or rarefaction corrections to the pressure measurements performed with the Pitot probe (Chue (1975), Menier (2007)). Although the outer diameter of the Pitot probe is of the same order of magnitude as the boundary layer thickness, by moving the Pitot probe by less than $1\,mm$ between each measurement point and thus, overlapping the measurements, accurate pressure profiles are obtained by calculating a moving average. The validity of this method was verified by Menier et al (2006) on a similar experimental setup. Furthermore, many studies related to high speed rarefied flows show that it is possible to capture these phenomena if the spatial resolution of the measurement is sufficiently refined (for instance, see Allègre and Bisch (1968)). In addition, because of the relatively large size of the Pitot tube compared to the flow phenomena, all measurements are referenced with respect to the center of the Pitot tube.

2.3.2 iCCD camera visualization

The flow around the flat plate is visualized with a PI-MAX Gen-II iCCD camera (1024×1024-pixel array) equipped with a VUV objective lens ($94\,mm$, $f/4.1$). The light is col-

lected through a fluorine window located in the wall of the test section chamber as shown on Fig. 4 (see Joussot et al (2015) for further details on the optical arrangement). Due to the rarefaction level of the flow, the natural flow field around the plate is experimentally visualized through the rarefied flow visualization technique. A description of this visualization method can be found in Fisher and Bharathan (1973). This technique allows shock waves to be distinguished in low density flows, where other techniques, for instance Schlieren, cannot be applied because of the low density of the flow. The rarefied flow visualization technique consists in using an electric discharge to weakly ionize the air flowing around a model in the test chamber. In this study, a voltage is applied between two parallel rectangular copper plates separated by a gap of about $300\,mm$. The flat plate is placed between these large electrodes, leading to a stream of ionized air around the model. The consecutive diffuse light emission is focused on the iCCD camera. Due to air density variations in the shock wave, a change in the light intensity in the resulting picture allows the shock wave to be detected (see Fig. 7). This technique is applied to analyze the flow field in the natural case (without the plasma discharge). When the plasma actuator is used, this technique is not employed because the bright visible emission of the discharge itself suffices to visualize the flow around the flat plate and the shock wave.

2.3.3 Surface temperature measurement

The evolution of the surface temperature of the flat plate is monitored with an infrared thermography device. The IR device is used to measure the flat plate surface temperature during the experiments. The IR camera (FLIR ThermaCAM SC 3000) is placed on the top of the wind tunnel (see Fig. 4) and focuses on the entire surface of the flat plate through a fluorine window compatible with the IR wavelength range of the camera. The IR camera is equipped with a QWIP-type IR photo-detector composed of a $(320 \times 240\text{-pixel array})$. As the emissivity of the electrodes is low ($\varepsilon < 0.1$ for bare aluminum foil), two black lines are painted on the flat plate surface. The method is detailed in Joussot et al (2015).

3 The baseline flows

3.1 DISIRAF code: baseline flow simulations

The Direct Simulation Monte Carlo (DSMC) is a method developed by Bird (1994) . It consists in a probabilistic simulation of the flow in which molecules mean free paths are in the same order as a representative physical length scale. It does not include any hypothesis linked to the form of the distribution functions and therefore, it can cope with flows arbitrarily far from equilibrium. The DISIRAF code (Direct SImulation of RArefied Flows) based on the DSMC method
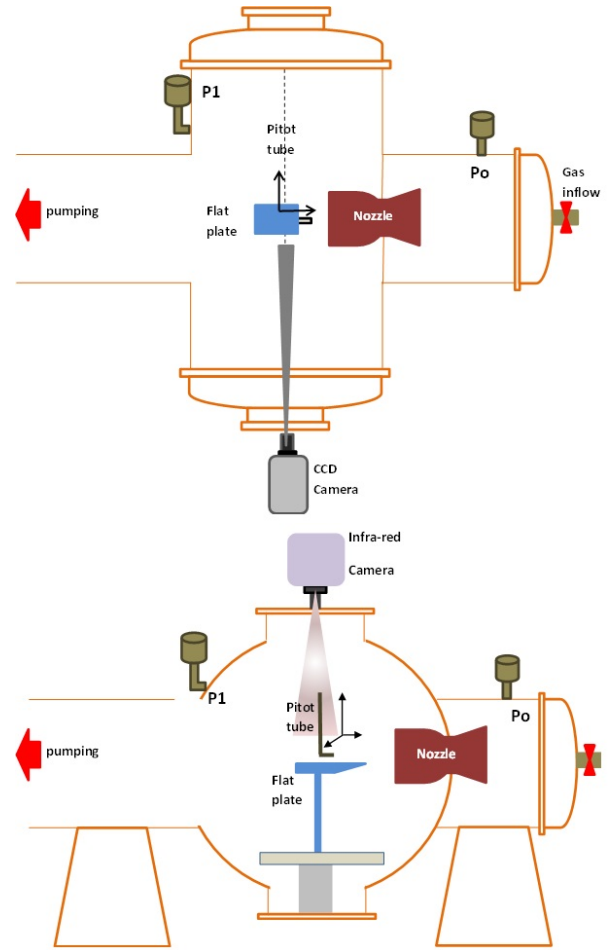

Fig. 4 Schematic view of the wind tunnel and configuration of the diagnostics

was developed at the ICARE laboratory (Lengrand (1991); Raffin (1994); Menier et al (2006)). It is adapted to compute stationary rarefied flows and is very efficient to solve aerodynamic problems in the transition regime, intermediate between the continuum and the free-molecular regimes (Tsuboi and Matsumoto (2001)). Macroscopic gas properties (viscosity, relaxation times, expressions for velocity slip and temperature jump) are consistent with descriptions at a molecular scale (cross-sections, transition probabilities, molecular collisions). Intermolecular collisions are modeled by Bird's VHS (Variable Hard Sphere) model. When conditions allow a viscosity to be defined, this model is coherent with a $\mu \propto T^{\omega}$ viscosity law. In the present study, only rotational and translational energies are considered. These rotational-translational energy exchanges during molecular collisions are handled by the Borgnakke-Larsen model, (Borgnakke and Larsen (1975)), using the formulation of Bird . The model boundary is divided into small regular surface elements. Momentum and energy exchanges due to the reflection of gas molecules are stored for each element individually. According to Maxwell's model, impinging molecules have a proba-
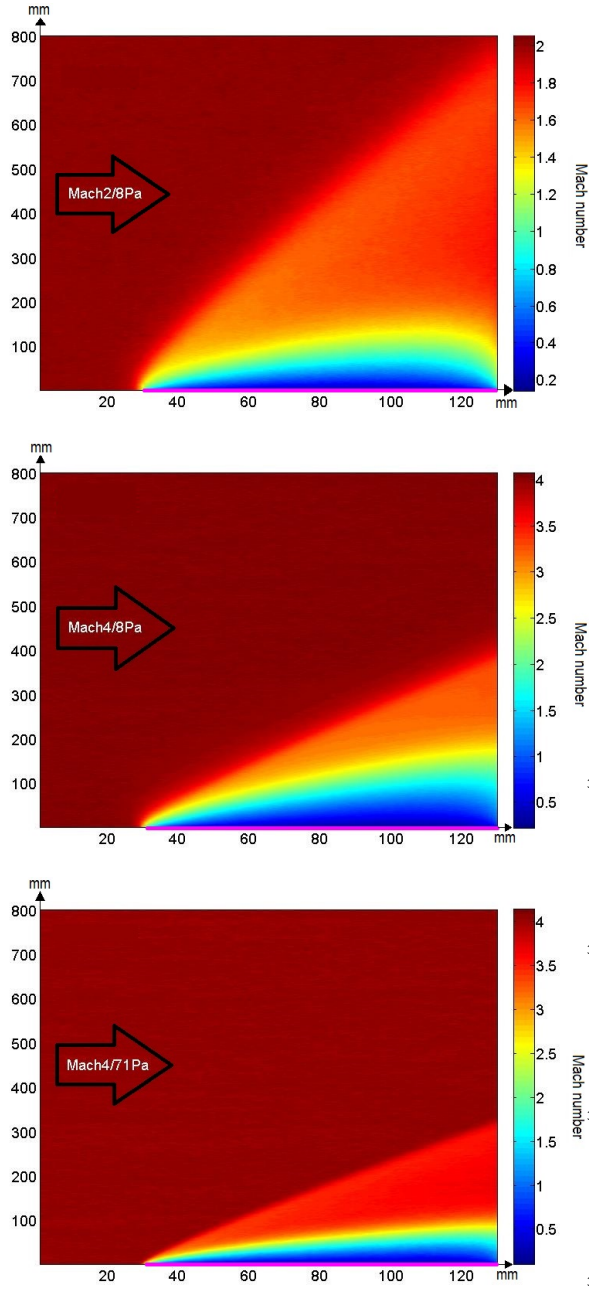
Fig. 5 DSMC Mach number flowfields for nozzles N1 (M2 - 8 Pa), N2 (M4 - 8 Pa) and N3 (M4 - 71 Pa). The upper surface of the flat plate is identified by a pink line

bility a to be reflected diffusely (with full accommodation at wall temperature) and a probability of $(1 - a)$ to be reflected specularly. To ensure the proper boundary conditions along the fluid boundaries of the computational domain, the code imposes the inward molecular flux through each boundary element according to the local values of flow density, temperature and velocity.

The Mach number flow fields calculated for each of the studied nozzles are presented on Fig. 5. The shock wave an-
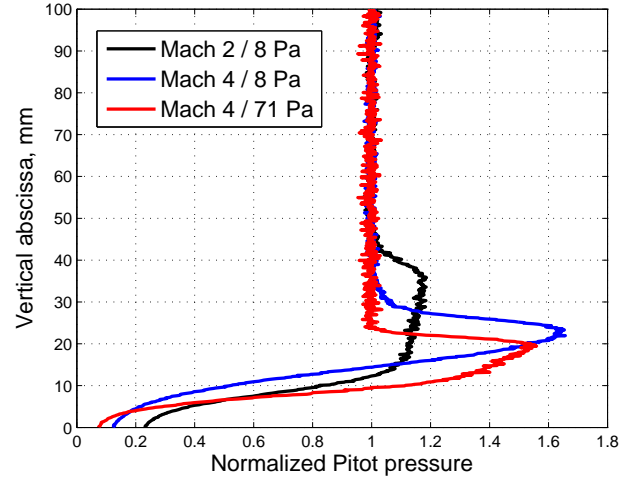
Fig. 6 Comparison of the numerical Pitot probe profiles calculated at $x = 50 mm$ for nozzles N1 (M2 - 8 Pa), N2 (M4 - 8 Pa) and N3 (M4 - 71 Pa)

gles β are determined from these mappings, as the angle between the tangent to the shock wave and the flat plate upper surface that coincides with the horizontal abscissa. On the flowfields (Fig. 5), the upper surface of the flat plate is identified by a pink line. The β values are: $36.9° \pm 0.5°$ for nozzle N1 (M2 - 8 Pa), $23.7° \pm 0.5°$ for nozzle N2 (M4 - 8 Pa) and $20.6° \pm 0.5°$ for nozzle N3 (M4 - 71 Pa).

As expected for the same static pressure $8 Pa$, when the Mach number increases the shock angle decreases. Concerning nozzles N2 and N3, working at the same Mach number (Mach 4) but different static pressures (respectively 8 Pa and 71 Pa), the shock angle decreases when increasing the static pressure because the boundary layer cannot expand and thus is less thick. Fig. 6 presents the Pitot probe profiles calculated at $x = 50 mm$ for each of the nozzles. These profiles are plotted in order to validate the values of the shock wave angles β found with the flowfields and especially when comparing the values with nozzle N3 (M4 - 71 Pa) to the experimental ones further in this paper. Indeed, one can notice a knee, typical of the region where the shock wave and the boundary layer are merged. Thus, the vertical abscissa of the knee for each curve represents the shock transition, making it possible to deduce the shock wave angle with a trigonometry formula.

3.2 Experimental baseline flows

The flow field around the flat plate was first investigated without any plasma discharge, corresponding to the study of the natural flow (namely, the baseline). The nominal operating conditions of the flow field remained those detailed in Table 1, Table 2 and Table 3 depending on the studied nozzle. Images obtained with the iCCD camera of the baseline

flow field are presented on Fig. 7 and Fig. 8, respectively for nozzles N1 (M2 - 8 Pa) and N2 (M4 - 8 Pa). In this case, the shock wave is experimentally visualized with the luminescent discharge technique (see sect. 2.3.2). These images result from the averaging and post-processing of 300 snapshots of the flow field recorded with the iCCD camera. The contrast is enhanced with ImageJ software in order to distinguish the shock wave position more precisely than is possible from a single raw image. The contrast of the picture allows to determine the shock wave shape. However, this technique is not effective when using the nozzle N3 (M4 - 71 Pa) as the static pressure of the generated flow is ten times higher than for the other nozzles. This leads the plasma to remain confined around the copper plate. When using the N1 (M2 - 8 Pa) nozzle, the shock wave can be fitted with a hyperbolic equation (Joussot et al (2015)). The shock wave angle β is then deduced from the hyperbola asymptote. For each experimental condition, the mathematical analysis was applied to a large number of images in order to average the angle value and estimate the standard deviation. For the baseline, the value of the shock wave angle is $\beta = 36.4° \pm 0.5°$. The analysis method is sufficiently sensitive to detect that the shock wave is slightly detached by $1 - 2\,mm$ from the leading edge of the plate because of the rarefaction effects. The N2 (M4 - 8 Pa) generates a Mach 4 flow at the same free stream pressure of 8 Pa. In this case, the shock wave is attached to the flat plate leading edge and cannot be fitted by a hyperbolic equation but by a linear one. Indeed, there is not the curved shape induced by the dilatation of the boundary layer that is observed for the N1 (M2 - 8 Pa) flow and here, the shock wave can be qualified as sharp. The shock wave angle is $\beta = 23.2° \pm 0.5°$. For the N3 (M4 - 71 Pa) nozzle, as the technique to capture the iCCD images is not efficient, the baseline shock wave angle was estimated with the experimental Pitot vertical profiles. Fig. 9 shows, for each of the studied nozzles, the profiles of the Pitot probe pressure measured above the flat plate at the abscissa $x = 50\,mm$ because at this position the pressure Pitot gradients are significant enough to be captured. The shape of the profiles shows a knee, typical of the region where the shock wave and the boundary layer are merged. The vertical abscissa of the knee for each curve represents the shock transition, from which the influence of the Mach number on nozzle N1 (M2 - 8 Pa) and N2 (M4 - 8 Pa) can be easily seen. The pressure gradient is less significant for lower Mach number but the pressure peak is found at a higher vertical position, thus leading to a greater shock wave angle. Then, the effect of the static pressure can be observed by comparing the curves for nozzles N2 (M4 - 8 Pa) and N3 (M4 - 71 Pa): for nozzle N3 (M4 - 71 Pa), the boundary layer is thinner because of a higher static pressure. For the nozzles N1 (M4 - 8 Pa) and N3 (M4 - 71 Pa), the experimental profiles are in good agreement with those calculated with the DISIRAF code (see Fig. 6).
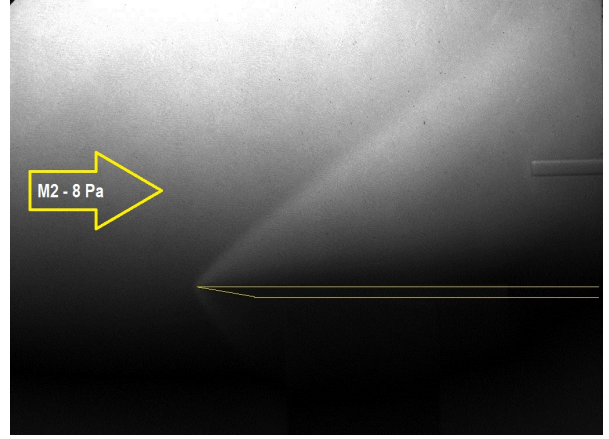

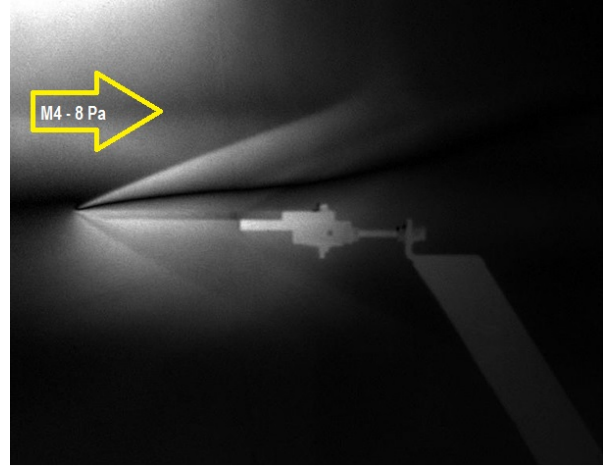**Fig. 7** Experimental baseline flow field obtained with the iCCD images with nozzle N1 (M2 - 8 Pa)

Fig. 8 Experimental baseline flow field obtained with the iCCD images with nozzle N2 (M4 - 8 Pa)

For the N2 (M4 - 8 Pa) nozzle, the boundary layer shape is not well reproduced by the simulation which suggests that the DISIRAF code has to be improved in order to better reproduce the shock wave for high Mach numbers. However, the z-position of the pressure peak is coherent with the numerical plot and this is precisely what was expected when doing the simulations, in order to validate the experimental shock wave angle values. Therefore, the shock wave angle can still be estimated with the same method as applied to the numerical Pitot pressure profile giving for N3 (M4 - 71 Pa), an experimental shock angle of $\beta = 20.8° \pm 0.7°$.

4 The plasma actuator effects

4.1 The plasma discharge characterization

The discharge is created by applying a negative DC potential to the active electrode. Fig. 10 and Fig. 11 present two pictures illustrating the discharge acting over the flat plat with
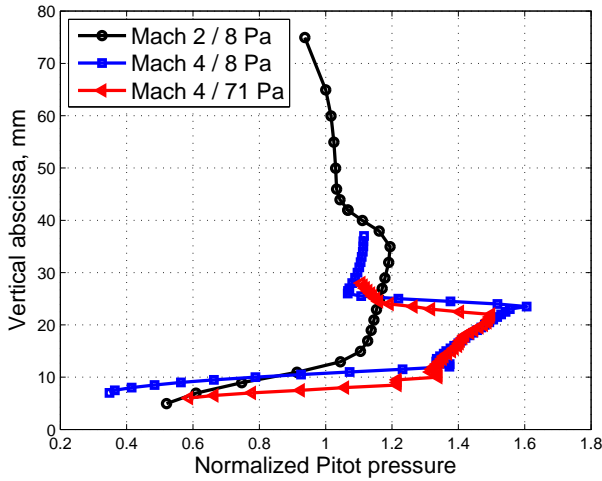
Fig. 9 Comparison of the experimental Pitot probe profiles measured at $x = 50\,mm$ for nozzles N1 (M2 - 8 Pa), N2 (M4 - 8 Pa) and N3 (M4 - 71 Pa)
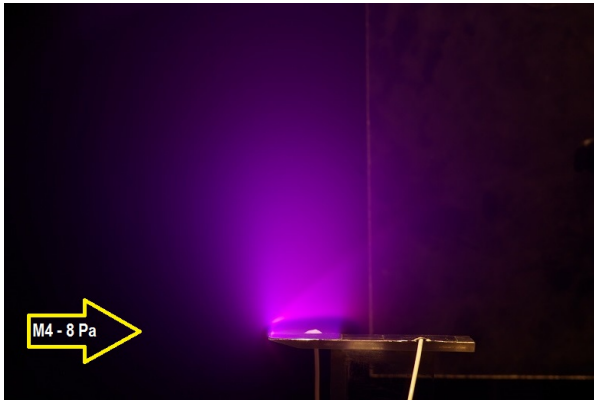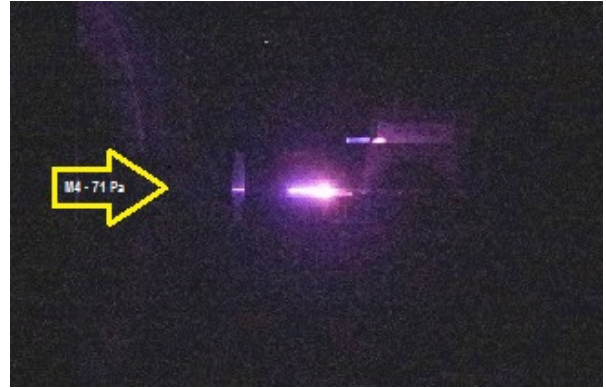

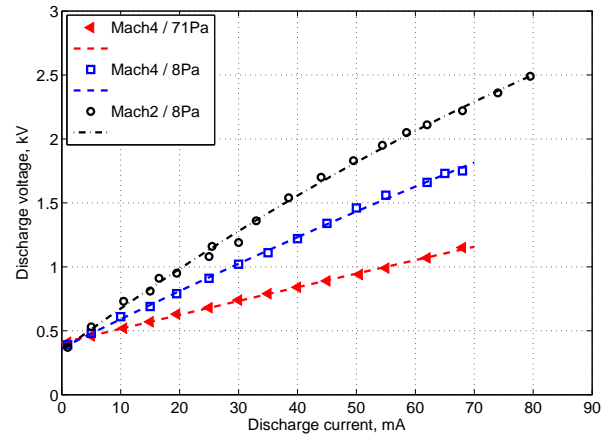**Fig. 11** Picture of the flat plate with discharge for the nozzle N3 (M4 - 71 Pa)

Fig. 12 Current-voltage characteristics of the plasma actuator for the three nozzles N1 (M2 - 8 Pa), N2 (M4 - 8 Pa) and N3 (M4 - 71 Pa)

Fig. 10 Picture of the flat plate with discharge for the nozzle N2 (M4 - 8 Pa)

nozzles N2 (M4 - 8 Pa) and N3 (M4 - 71 Pa) respectively. The nozzle N1 (M2 - 8 Pa) flow is not plotted because the discharge resembles that of the N2 (M4 - 8 Pa) one. As observed, the behavior of the discharge is completely different and strongly depends on the working pressure. When using nozzles N1 (M2 - 8 Pa) and N2 (M4 - 8 Pa), the discharge is diffused and extends over a large region because the discharge connects to the ground via the wall of the wind tunnel. But when increasing the working pressure with nozzle N3 (M4 - 71 Pa) the plasma is confined over the two electrodes on the plate.

For each flow configuration the electrical behavior discharge was analyzed from the voltage and current discharge measurements. Fig. 12 shows the current-voltage (I_{HV}-V_{HV}) characteristics of the plasma actuator for the three operating flow conditions and the corresponding power discharge. The discharge ignition voltage is quite similar, ranging from $V_{HV} = -0.36\,kV$ for N1 to $V_{HV} = -0.40\,kV$ for nozzles N2

(M4 - 8 Pa) and N3 (M4 - 71 Pa). For any of the three nozzles the discharge current increases with the applied voltage, corresponding to the abnormal glow discharge regime (Phelps (2001)). Nevertheless for a given discharge voltage, the current increases with the Mach number and with the working pressure. From this, one can deduce the power consumption, since for the same applied voltage, less power is used when increasing the Mach number and the static pressure. For example, when applying $60\,mA$ to the discharge power is twice that with nozzle N1 (M2 - 8 Pa) compared to nozzle N3 (M4 - 71 Pa).

An iCCD image obtained with nozzle N2 (M4 - 8 Pa)and a current discharge of $55\,mA$ is presented on Fig. 13. To improve the visualization of the shock wave the contrast of the original figure is enhanced with ImageJ. Qualitatively the same description applies to nozzles N1 (M2 - 8 Pa) and N2 (M4 - 8 Pa). The gas above the flat plate is weakly ionized when the discharge is on. Visually, it corresponds to the luminous area, which exhibits a plume–like shape slightly slanted in the upstream direction.
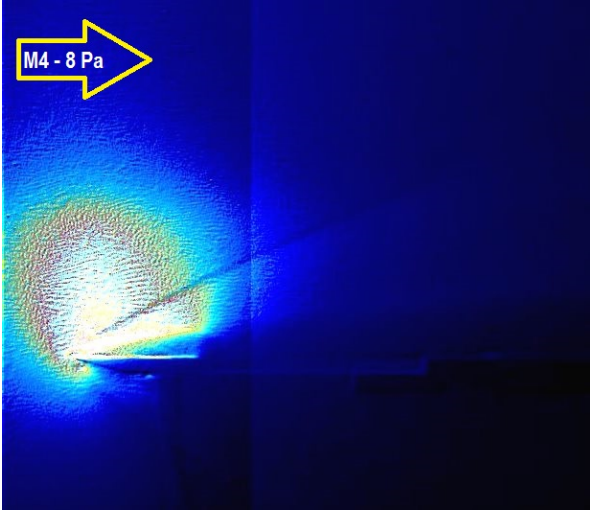
Fig. 13 Visualization of the N2 (M4 - 8 Pa) shock wave with 55mA discharge current applied on the plasma actuator

Nozzle N3 (M4 - 71 Pa) generates a flow field at a static pressure almost ten times higher than the other two nozzles. The main consequence is that the discharge pattern is highly contrasted and remains very confined as if flattened on the model surface, as can be observed on Fig. 14.

Furthermore, the discharge reattaches the grounded electrode denoting a completely different behavior to that than those occurring with nozzles N1 (M2 - 8 Pa) and N2 (M4 - 8 Pa) flows where the discharge diffuses in the upstream direction and makes the grounded electrode useless. This behavior is due to the mean free path value, that is consequently lower with nozzle N3 (M4 - 71 Pa) than for N1 (M2 - 8 Pa) and N2 (M4 - 8 Pa) because of the higher static pressure. Two distinct zones can be observed, a purple area close to the leading edge and a magenta one close to the grounded electrode, denoting the presence of different excited species. Also, the plasma begins to be created between the grounded electrode (on the left) and the cathode. Then with the increase in the current discharge the plasma extends toward the leading edge, becoming more luminous and thicker.

4.2 Shock wave angle modifications

In previous work carried out with nozzle N1 (M2 - 8 Pa), it was observed that the increase in the discharge current applied to the active electrode reflects an increase of the shock wave angle. Similar behavior is observed with nozzles N2 (M4 - 8 Pa) and N3 (M4 - 71 Pa). The iCCD images obtained with nozzle N2 (M4 - 8 Pa) clearly shows a modification of the shock wave angles. To illustrate this, Fig. 15 and Fig. 16 present the comparison of shock waves measured for two distinct discharge currents applied to the electrode $I_{HV} = 40\,mA$ and $I_{HV} = 62\,mA$ and acquired during the same
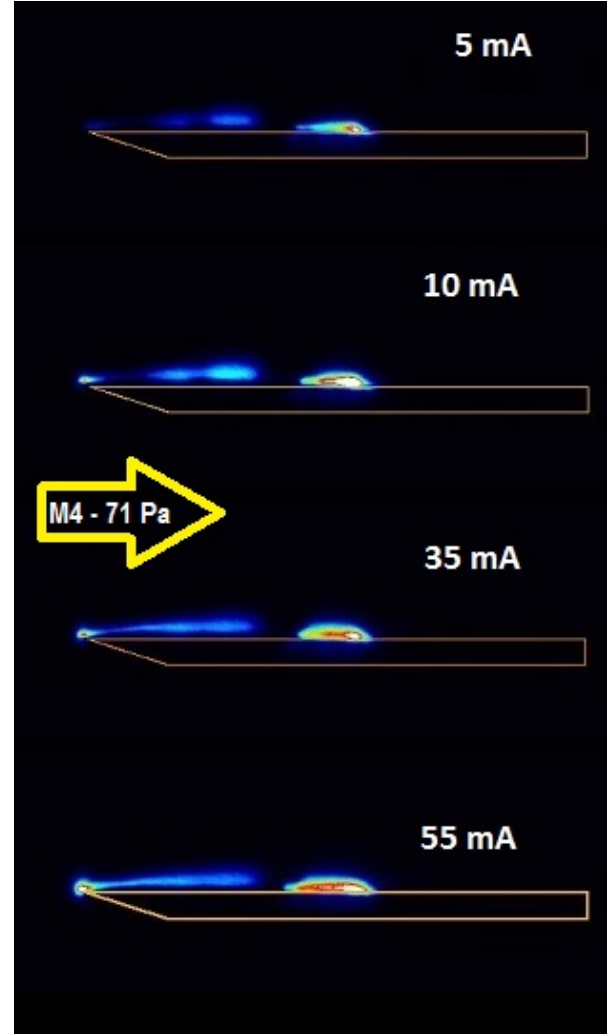

Fig. 14 Visualization of the discharge created with nozzle N3 (M4 - 71 Pa) at different current discharge values

series of experiments meaning that the experimental setup is unchanged.

Fig 15 presents a comparison of the shock wave shape measured for the two different discharge currents in the region close to the leading edge. It can be clearly observed that at higher discharge current the shock wave shape is rounded while the baseline shock wave is sharp. A dark area above the cathode appears, corresponding to the plasma sheath which merges with the boundary layer of the flow field. This modification induced by the plasma discharge also deflects the shock wave outward from the flat plate surface and obviously, this leads to the increase in the shock wave angle β. Fig. 16 presents the overlaying of the iCCD images obtained for $I_{HV} = 40\,mA$ and $I_{HV} = 62\,mA$. The contrast of iCCD images is enhanced in order to bring out the end of the shock wave shape and makes it possible to observe the sharp increase of the shock angle defined by the dark margin. The shock waves angles are determined from
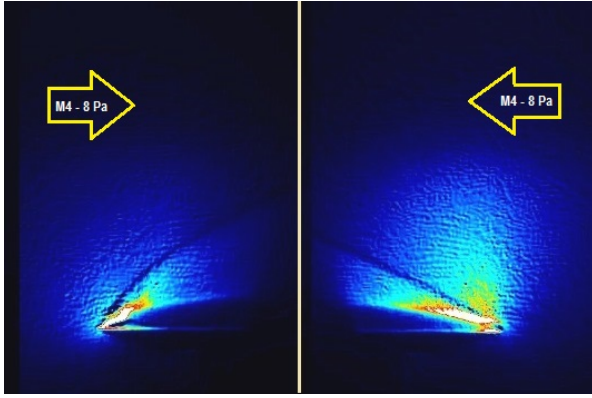
Fig. 15 Comparison of shock wave shapes with nozzle N2 (M4 - 8 Pa) for two different current discharges: 40*mA* (rigth) and 62*mA* (left)
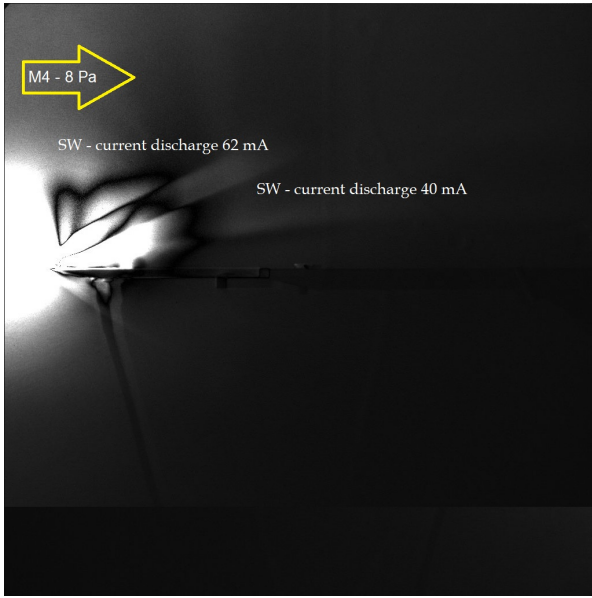

Fig. 16 Visualization of the shock wave modification with the increase of discharge current with nozzle N2 (M4 - 8 Pa)

Fig. 17 Effect of the plasma discharge on the Pitot probe profiles measured at $x = 50\,mm$ for nozzle N2 (M4 - 8 Pa)

Fig. 18 Temperature profiles along the x axis of the flat plate measured for the nozzle N2 (M4 - 8 Pa)

the iCCD images with the method explained in section 2.3.2.

Vertical Pitot probe profiles were measured at $x = 50\,mm$ from the leading edge for three current discharge values $I_{HV} = 10\,mA$, $I_{HV} = 35\,mA$ and $I_{HV} = 55\,mA$. Results are presented on Fig. 17. Compared to the baseline profile, the pressure profiles are all shifted at higher z values as the discharge current increases. This effect not only confirms the increase in the shock wave angle, but also shows the thickening of the boundary layer with the discharge current as it was already observed for nozzle N1 (M2 - 8 Pa). In the case of rarefied flow regime, one of the main effects expected to be responsible for the shock wave modification is the heating of the model surface Semenov et al (2002); Menart et al (2004); Bletzinger et al (2005), which induces a displacement effect Hayes and Probstein (1966). The flow viscosity above the heater is modified, leading to an increase in the boundary
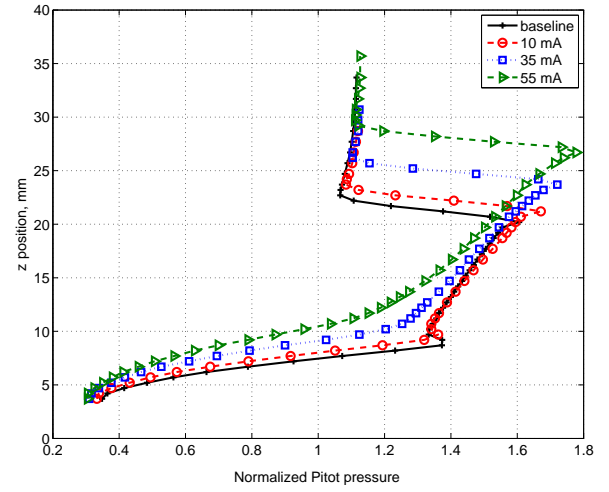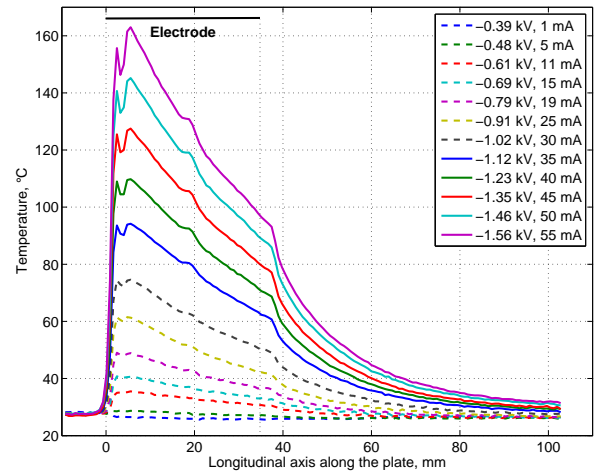
layer thickness, and, consequently, a shifting of the shock wave outward from the flat plate surface (i.e., β increases) (Kinefuchi et al (2016)).

To quantify the impact of the heating, the temperature of the surface plate was measured with the infrared camera for several discharge current values applied to the plasma actuator as described in section 2.3.3. The temperature distribution along the longitudinal axis of the plate is plotted on Fig. 18. It is clear that the model surface is heated by the plasma actuator. The temperature values increase with the discharge current applied to the actuator. This explains why the region where the temperature values are the greatest corresponds to the region occupied by the cathode, reaching even higher values at the leading edge because the electric field values is there the strongest. This observed behavior is similar to
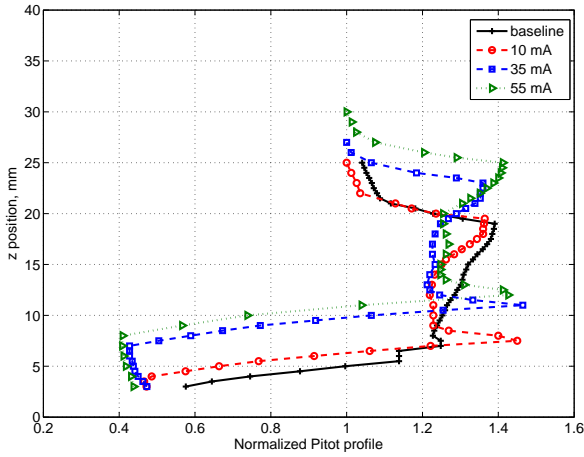
Fig. 19 Effect of the plasma discharge on the Pitot probe profiles at $x = 50\,mm$ for the nozzle N3 (M4 - 71 Pa)

Fig. 20 Temperature profiles along the x axis of the flat plate measured for the nozzle N3 (M4 - 71 Pa)

that obtained with the nozzle N1 (M2 - 8 Pa). Nevertheless the temperatures reached for the same discharge power are lower with the nozzle N2 (M4 - 8 Pa) compared to the nozzle N1 (M2 - 8 Pa). Knowing that for the N1 (M2 - 8 Pa) nozzle the increase in the shock wave angle is half due to the surface heating and half to the ionization, it can be assumed that for the nozzle N2 (M4 - 8 Pa) the latter effect is more significant. For the nozzle N3 (M4 - 71 Pa), the effect of the plasma actuator is captured from Pitot probe profiles plotted on Fig. 19 and measured at the inter electrode space at abscissa $x = 50\,mm$ Compared to the baseline profile, the discharge created by the plasma actuator also induces a thickening of the boundary layer, pushing the shock wave upward. The most visible effect occurs for the discharge current passing from $I_{HV} = 10\,mA$ to $I_{HV} = 35\,mA$ because for this discharge current value, the plasma layer over the active electrode reaches the leading edge recovering the sharp leading edge as can be seen on Fig. 14.

Indeed, there is an extension of the plasma layer from the grounded electrode toward the leading edge. This can also be noticed from the plate surface temperatures measured with the infrared camera and plotted on Fig. 20. The development of the plasma layer along the plate with the discharge current reflects the temperature evolution. For low discharge current values, the plasma starts close to the grounded electrode and thus, the temperature profile is maximum in this region. Then, as observed on the figure, the temperature peak moves toward the leading edge when increasing the discharge current. For example, the values range from $36^\circ C$ at $35\,mA$ to $47^\circ C$ for $55\,mA$. However, even the highest temperatures reached remain low compared to those measured for nozzles N1 (M2 - 8 Pa) and N2 (M4 - 8 Pa).
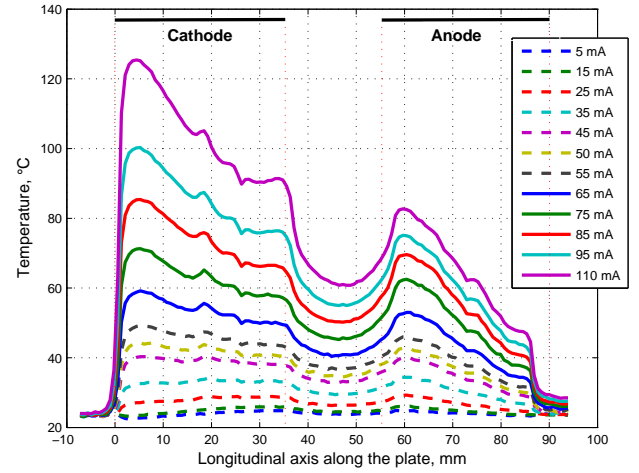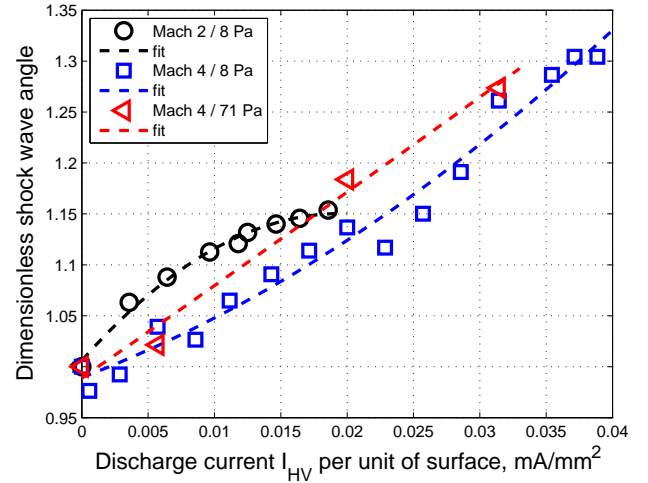

Fig. 21 Dimensionless shock wave angles versus the discharge current per unit of surface for the three nozzles N1 (M2 - 8 Pa), N2 (M4 - 8 Pa) and N3 (M4 - 71 Pa)

4.3 Results and discussion

Shock wave angles were determined from the the iCCD images for nozzles N1 (M2 - 8 Pa) and N2 (M4 - 8 Pa) and from the Pitot profiles for nozzle N3 (M4 - 71 Pa). Fig. 21 plots the dimensionless angles with respect to their respective baseline values versus the discharge current per unit of surface for the three nozzles.

With respect to the baseline angle values, the plasma actuator induces a greater increase in the shock wave angle for nozzles N2 (M4 - 8 Pa) and N3 (M4 - 71 Pa), although the baseline shock wave angle is smaller with these nozzles. Therefore, when doubling the Mach number, the effects of the plasma actuator are even greater. When increasing the plasma actuator discharge current from $I_{HV} = 1\,mA$
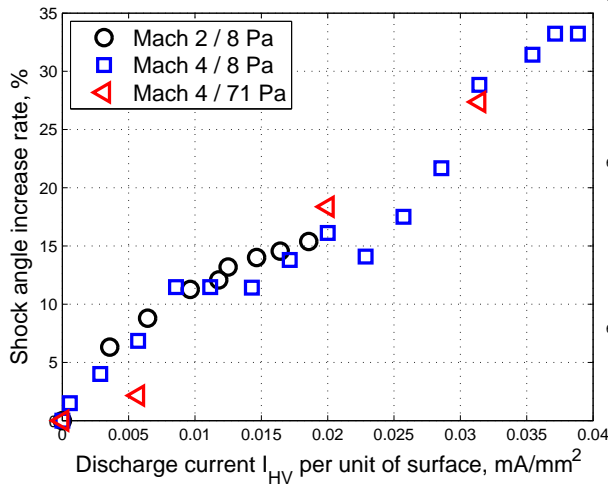
Fig. 22 Comparison of the shock angle increase rate versus the discharge current per unit of surface for the three nozzles N1 (M2 - 8 Pa), N2 (M4 - 8 Pa) and N3 (M4 - 71 Pa)

to $I_{HV} = 50\,mA$, the baseline shock wave angle increases by 1.15 with nozzle N1 (M2 - 8 Pa) while for the same conditions, the baseline shock wave angle increases by 1.21 when using the N2 (M4 - 8 Pa) nozzle and by 1.28 for the N3 (M4 - 71 Pa) nozzle. Another way to analyze the plasma actuator effects is presented on Fig. 22, where the angle increase ratio is represented in terms of percentage. For discharge currents up to $40\,mA$ the shock wave angle increase behaves in the same way whatever the nozzle used, then the curve corresponding to nozzle N1 (M2 - 8 Pa) seems to tend to a limit while for the other two nozzles it continuous to increase. For the nozzle N3 (M4 - 71 Pa), despite the thinner boundary layer compared to the other two nozzles, the increase rates of the shock wave angle are equivalent to those obtained with the nozzle N2 (M4 - 8 Pa).

Furthermore, in terms of power consumption, the plasma actuator consumes less at higher Mach number and higher working pressure. That means that the plasma actuator is more efficient for nozzle N3 (M4 - 71 Pa) air flow conditions and the effectiveness increases with the discharge current. This result is due to the value of the mean free path obtained for the operating conditions of each nozzle. The mean free path for nozzle N1 (M2 - 8 Pa) is 8.37 times the one for nozzle N2 (M4 - 8 Pa) and 32 times the mean free path of nozzle N3 (M4 - 71 Pa). As a consequence, the collisions between molecules are more efficient for smaller mean free path values and the plasma volume created by the discharge will also be smaller decreasing the energy consumption for a given discharge current. That said, the discharge current developed by the actuator is relevant to the ionization rate, so one can consider that for a given power-discharge, the ionization rate for the nozzle N3 (M4 - 71 Pa) should be higher than those of nozzles N2 (M4 - 8 Pa) and N1 (M2 - 8 Pa).

Considering this assumption and the fact that the surface temperatures are lower for the nozzle N3, one can conjecture that the plasma actuator is more interesting for higher velocities and pressures because the ionization effect seems to be more significant than the surface heating effect. Still concerning the nozzle N3 (M4 - 71 Pa), the boundary layer thickness 'jump' observed on Fig. 19 between $I_{HV} = 10\,mA$ and $I_{HV} = 35\,mA$, suggests the behavior of the boundary layer obtained with a blunt flat plate in a rarefied regime, since for the other nozzles the increase in the boundary layer thickness with the discharge current is continues and does not show this kind of gap. Several studies have been carried out to study the boundary layer displacement and leading edge bluntness effects in supersonic and hypersonic flow. Cheng (2012) suggests a theory verified with experiments where he shows that at low Reynolds number, the boundary layer displacement thickness increases with the effective model leading edge thickness and thus pushes out the shock wave. Similar conclusions were drawn by Jean Allegre in Allègre et al (1994) and Allègre and Bisch (1968). In the present case, it is as if the plasma formed over the plate acts like a blunt body when it recovers the leading edge (see Fig. 14) and the global geometry encountered by the flow resembles a blunted plate whose radius edge thickness increases with the plasma discharge current.

5 Conclusions

This experimental work focused on the study of the influence of Mach number and static pressure on the effects of plasma flow control. Previous work has shown the efficiency of a plasma discharge on the increase in the shock wave angle created over a sharp plate interacting with a Mach 2 - 8Pa flow. Also, the set of experiments carried out helped to understand how the plasma discharge interacts with the flow field and what the plasma properties involved in the observed mechanisms are. The observations determined that in such a configuration, half of the angle increase was due to the surface heating induced by the plasma and the other half was due to the ionization rate of the flow surrounding the flat plate.

In the present work, the investigation emphasizes the influence of the flow itself on the plasma actuator. To this end, two other nozzles N2 (M4 - 8Pa) and N3 (M4 - 71 Pa) were used, in order to analyze both the influence of the Mach number and the influence of the static pressure. Baseline shock waves are different according to the flow conditions, as the hyperbolic shock wave angle found with the N1 (M2 - 8 Pa) nozzle becomes sharper with Mach 4 nozzles, and moreover, the shock wave angle decreases at higher Mach number and higher static pressures. In this respect, the plasma actuator has a significant influence with the increase of Mach number and static pressure.

Results have shown that in the range of the discharge current applied to the plasma actuator ($1\,mA$ to $50\,mA$), the shock wave angle increases by 1.15 with the nozzle N1 (M2 - 8 Pa) and by 1.21 and 1.28 with the nozzles N2 (M4 - 8 Pa) and N3 (M4 - 71 Pa) respectively. It is interesting to note that the power consumption decreases when increasing the static pressure. This effect is due to the mean free path which decreases with the Mach number and with the pressure.

The morphology of the plasma discharge strongly depends on the static pressure. For a static pressure of $8\,Pa$, the plasma is very diffused and extends in the upstream direction while it is confined to the flat plate surface and reattaches to the grounded electrode for the flow at $71\,Pa$. For this condition, the plasma actuator produces a thin layer of plasma over the plate surface producing a bluntness effect on the sharp flat plate. Furthermore, it is observed with nozzle N3 (M4 - 71 Pa), that different excited species are present depending on whether one considers the cathode or the anode, but this point will be studied in detail in further experiments with a detailed optical spectroscopy analysis. Future work will focus on electrostatic probe measurements that should lead to the quantification of the ionization rate and a better understanding of the coupling between the flow speed and the collision time between electrons and molecules.

References

Allègre J (1992) The SR3 low density wind-tunnel. Facility capabilities and research development. In: AIAA Paper No. 92–3972

Allègre J, Bisch C (1968) Angle of attack and leading edge effects on the flow about a flat plate at mach number 18. AIAA Journal 6(5):848–852

Allègre J, Raffin M, Chpoun A, Gottesdiener L (1994) Rarefied hypersonic flow over a flat plate with truncated leading edge. Progress in Astronautics and Aeronautics 160:285–285

Atkinson M, Poggie J, Camberos J (2013) Control of high-angle-of-attack reentry flow with plasma actuators. Journal of Spacecraft and Rockets 50(2):337–346

Bird GA (1994) Molecular Gas Dynamics and the Direct Simulation of Gas Flows. Oxford University Press, New York

Bletzinger P, Ganguly BN, van Wie D, Garscadden A (2005) Plasmas in high speed aerodynamics. J. Phys. D: Appl. Phys.38(4):R33–57

Borgnakke C, Larsen PS (1975) Statistical collision model for monte carlo simulation of polyatomic gas mixture. Journal of computational Physics 18(4):405–420

Cheng H (2012) Boundary-layer displacement and leading-edge bluntness effects in high-temperature hypersonic flow. Journal of the Aerospace Sciences

Chue SH (1975) Pressure probes for fluid measurement. Prog Aerosp Sci 16(2):147–223

Coumar S, Joussot R, Parisse JD, Lago V (2015) Effect of surface heating on shock wave modification by a plasma actuator in a rarefied supersonic flow over a flat plate. In: 20th AIAA International Space Planes and Hypersonic Systems and Technologies Conference, p 3562

Coumar S, Joussot R, Parisse JD, Lago V (2016) Influence of a plasma actuator on aerodynamic forces over a flat plate interacting with a rarefied mach 2 flow. International Journal of Numerical Methods for Heat & Fluid Flow 26(7):2081–2100

Fisher SS, Bharathan D (1973) Glow-discharge flow visualization in low-density free jets. J. Spacecraft Rockets10(10):658–62

Hayes WD, Probstein RF (1966) Hypersonic flow theory, Vol. I Inviscid flows. Academic Press, New York

Joussot R, Lago V (2016) Experimental investigation of the properties of a glow discharge used as plasma actuator applied to rarefied supersonic flow control around a flat plate. IEEE Transactions on Dielectrics and Electrical Insulation 23(2):671–682

Joussot R, Lago V, Parisse JD (2015) Quantification of the effect of surface heating on shock wave modification by a plasma actuator in a low-density supersonic flow over a flat plate. Experiments in Fluids 56(5):1–18

Kimmel RL, Hayes JR, Menart JA, Shang J (2004) Effect of surface plasma discharges on boundary layers at mach 5. In: AIAA Paper No. 2004-0509

Kinefuchi K, Starikovskiy A, Miles R (2016) Control of shock wave-boundary layer interaction using nanosecond dielectric barrier discharge plasma actuators. In: 52nd AIAA/SAE/ASEE Joint Propulsion Conference, p 5070

Kuo SP (2007) Plasma mitigation of shock wave: experiments and theory. Shock Waves 17(4):225–39

Kuo SP, Bivolaru D (2007) The similarity of shock waves generated by a cone-shaped plasma and by a solid cone in a supersonic airflow. Phys. Plasmas14(2):023,503 (5 pp.)

Lago V, Lengrand J, Menier E, Elizarova T, Khokhlov A, Abe T (2008) Physical interpretation of the influence of a dc discharge on a supersonic rarefied flow over a flat plate. In: Aip Conference Proceedings, vol 1084, p 901

Lago V, Joussot R, Parisse J (2014) Influence of the ionization rate of a plasma discharge applied to the modification of a supersonic low reynolds number flow field around a cylinder. Journal of Physics D: Applied Physics 47(12):125,202

Lengrand JC (1991) Dsmc calculation of a compression corner flow. Aerothermodynamics for Space Vehicles

Leonov SB (2011) Review of plasma-based methods for high-speed flow control. AIP Conf Proc 1376:498–502

Leonov SB, Yarantsev DA (2008) Near-surface electrical discharge in supersonic airflow: Properties and flow control. J. Propul. Power24(6):1168–81

Leonov SB, Yarantsev DA, Gromov VG, Kuriachy AP (2005) Mechanisms of flow control by near-surface electrical discharge generation. In: AIAA Paper No. 2005–780

Menart J, Handerson S, Atzbach C, Shang J, Kimmel R, Hayes J (2004) Study of surface and volumetric heating effects in a mach 5 flow. In: AIAA Paper No. 2004-2262

Menart J, Stanfield S, Shang J, Kimmel R, Hayes J (2006) Study of plasma electrode arrangements for optimum lift in a mach 5 flow. In: 44th AIAA Aerospace Sciences Meeting and Exhibit, p 1172

Menier E (2007) Influence d'une décharge électrique continue sur un écoulement supersonique raréfié. PhD thesis, Université d'Orléans, France

Menier E, Lengrand JC, Depussay E, Lago V, Leger L (2006) Direct simulation monte carlo method applied to the ionic wind in supersonic rarefied conditions. AIAA paper (2006-3343)

Menier E, Leger L, Depussay E, Lago V, Artana G (2007) Effect of a dc discharge on the supersonic rarefied air flow over a flat plate. J. Phys. D: Appl. Phys.40(3):695–701

Palm P, Meyer R, Pl'onjes E, Rich JW, Adamovich IV (2003) Nonequilibrium radio frequency discharge plasma effect on conical shock wave: M = 2.5 flow. AIAA J.41(3):465–9

Phelps A (2001) Abnormal glow discharges in ar: experiments and models. Plasma Sources Science and Technology 10(2):329

Poggie J (2005) Dc glow discharges: a computational study for flow control applications. In: 36th AIAA Plasmadynamics and Lasers Conference, p 5303

Raffin M (1994) Rarefied hypersonic flow over a sharp flat plate: numerical and experimental results. In: Rarefied Gas Dynamics: Technical Papers from the Proceedings of the Eighteenth International Symposium on Rarefied Gas Dynamics, University of British Columbia, Vancouver, British Columbia, Canada, July 26-30, 1992..., American Institute of Aeronautics and Astronautics, Incorporated, vol 160, p 276

Semenov VE, Bondarenko VG, Gildenburg VB, Gubchenko VM, Smirnov AI (2002) Weakly ionized plasmas in aerospace applications. Plasma Phys. Contr. F.44(12B):B293–305

Shin J, Narayanaswamy V, Raja L, Clemens NT (2007) Characteristics of a plasma actuator in mach 3 flow. In: AIAA Paper No. 2007–788

Starikovskiy A, Aleksandrov N (2011) Nonequilibrium Plasma Aerodynamics. INTECH Open Access Publisher

Surzhikov ST, Shang JS (2004) Two-component plasma model for two-dimensional glow discharge in magnetic field. Journal of Computational Physics 199(2):437–464

Tsuboi N, Matsumoto Y (2001) Dsmc simulation with gas-surface interaction models in hypersonic rarefied flow. In: AIP Conference Proceedings, IOP Institute OF Physics Publishing LTD, pp 331–338

Zuppardi G (2015) Aerodynamic control capability of a wing-flap in hypersonic, rarefied regime. Advances in aircraft and spacecraft science 2(1):45–56